

Momentum-Resolved Resonant Inelastic X-ray Scattering as a Novel Tool to Study the Bulk Electronic Structure of Complex Insulators

M.Z. Hasan¹, E.D. Isaacs², Z.-X. Shen¹, L.L. Miller³

¹*Dept. of Applied Physics, Physics & Stanford Synchrotron Radiation Laboratory (SSRL), Stanford Linear Accelerator Center (SLAC), Stanford University, Stanford, CA*

²*Bell Laboratories, Lucent Technologies, Murray Hill, NJ*

³*Dept. of Physics, Iowa State University & Ames Laboratory, Ames, IA*

The discovery of high temperature superconductivity and colossal magnetoresistance (CMR) in doped transition metal oxides has led to the extensive research interests in Mott insulators. Such oxides are characterized by large onsite Coulomb interaction and the consequent low-temperature insulating state characterized by a charge-excitation gap known as the Mott-gap. The gap is either set by the Coulomb interaction or the charge-transfer energy (energy to remove an electron from oxygen orbital and put it on a metal site) depending on which one is lower [1,2]. This suggests the importance of a thorough study of their correlated charge dynamics. Angle-resolved photoemission (ARPES), which probes the occupied electronic states in a momentum-resolved manner, has been successful in characterizing the electronic structure of these oxides [3,4], whereas, electron-energy-loss spectroscopy (EELS) is limited to low momentum transfers due to multiple scattering effects arising from its strong coupling nature [5]. Being surface sensitive, both ARPES and EELS require extensive ultra-high vacuum (UHV) sample preparation [3-5]. A study of the momentum-resolved bulk electronic structure, especially for the unoccupied bands, is absent for these correlated insulators.

Inelastic x-ray scattering (IXS) can be a useful probe of electronic excitations in condensed matter systems because of its fairly wide kinematic range and direct coupling to the electron charge [6-10]. Due to large absorption cross-sections in high density (high-Z) materials, applications of IXS have been mostly limited to low-Z systems. Recent experimental and theoretical/numerical investigations have shown that by tuning the incident energy near an x-ray absorption edge, a Raman-type effect could be measured with non-zero momentum transfer, despite the high absorption limitation, because of the large enhancement achieved near a resonance which eventually dominates the overall scattering cross-section [9-12]. The observation of a low-energy charge-transfer gap has been reported recently with non-zero \mathbf{q} (\mathbf{q} being the momentum transfer in units of $\hbar/2p$) in a parent cuprate, using inelastic x-ray scattering [10] and has been studied extensively

by optical spectroscopies (with $\mathbf{q} \sim 0$) [13]. A similar excitation band is also seen in EELS at low momentum transfers (< 1 inverse Angstrom) [5]. From work done at NSLS beamline X21, we have recently demonstrated that, in addition to being a direct probe of the anisotropy of charge excitation gaps, inelastic x-ray scattering data can yield momentum-resolved information about the unoccupied electronic states [11].

Experiments were performed at the X-21 wiggler beamline at the National Synchrotron Light Source of Brookhaven National Laboratory. The overall energy resolution was 0.45 eV and typical inelastic count rates from the sample were 20 to 30 counts per minute at energy losses of several electron volts. The scattered light was reflected from a germanium analyzer and focused onto a solid-state detector. Energy analysis was done by rotating the analyzer and translating the detector, accordingly, at the focus of the analyzer. The incident energy was kept fixed near the Cu K-edge ($E_0 = 8995.8$ eV).

Inelastic x-ray scattering spectra near the Cu K-edge from parent cuprate $\text{Ca}_2\text{CuO}_2\text{Cl}_2$, with varying momentum transfers along the $\langle 110 \rangle$ direction (45 degrees to the Cu-O bond direction), are shown in Fig. 1(A). Fig. 1(B) shows spectra with momentum transfers along the $\langle 100 \rangle$ (the Cu-O bond) direction. Elastic scattering has been removed by fitting and all of the spectra in each panel were normalized near 8 eV energy-loss so the intensities are relative. Each spectrum exhibits two features, a broad excitation band near 5.8 eV and a weak feature near 2.45 to 3.9 eV, for different \mathbf{q} values. The broad feature centered near 5.8 eV changes shape with different \mathbf{q} , but does not show any significant dispersion in either of the $\langle 110 \rangle$ or $\langle 100 \rangle$ directions. Nondispersive behavior exhibited by this feature over a large range of \mathbf{q} suggests that it has a local character. Based on electronic structure calculations, the 5.8 eV feature is believed to be a charge transfer excitation from an occupied state with b_{1g} symmetry to an empty state with a_{1g} symmetry [10,14]. The position of the lower energy feature, on the other hand, shows significant variation with changing \mathbf{q} , as seen in

Fig. 1(A). The feature disperses monotonically upwards about 1.4 eV in the $\langle 110 \rangle$ direction, but shows much less dispersion for momentum transfer along the $\langle 100 \rangle$ Cu-O bond direction. Dispersion behaviors for these two directions are compared in Fig. 2(A), which shows the center of gravity of the low-energy feature's spectral weight. Overall dispersion along the bond direction is much smaller than dispersion along the diagonal direction in the Cu-O lattice.

Inelastic x-ray scattering measures the dynamical correlation function (charge fluctuations), which can be interpreted as particle-hole pair excitations in the range of momentum transfers comparable to the size of the equivalent Brillouin zones of the system. In an insulator, for scattering near an absorption edge, the core-hole created by the X-ray photon causes electronic excitations in the valence band, which creates a hole in the occupied band and promotes an electron to the unoccupied band across the gap [7-12]. A likely scenario for the origin of the lower energy feature observed in our experimental data is that it consists of charge excitations across the characteristic gap in the system (the charge-transfer gap or effective Mott gap), which is related to the gap seen in optical experiments (~ 2 eV) [13]. In an effective single-particle band picture (this excitation [12] is shown in Fig. 2(B)) it is an excita-

tion from the occupied band to the unoccupied (upper Hubbard) band. In the case of a hole forming a pair with an electron, there would be different propagation probabilities along the Cu-O bond, and 45 degrees to the Cu-O bond, due to the antiferromagnetic correlation of the lattice (as shown in Fig. 2(C)) [5,11,12]. This difference can be relatively significant because of the large magnetic coupling exhibited by the undoped cuprate insulator. These results are consistent with numerical studies of the Hubbard Hamiltonian (Fig. 3), which goes beyond the single-particle band picture and includes on-site local Coulomb interactions among the electrons [11,12].

Our results demonstrate the feasibility of inelastic x-ray scattering to study electronic excitations at the gap edge of Mott insulators and its potential for gaining fundamental information about correlated electron systems. The momentum-resolved nature of the upper Hubbard band of charge-transfer, or Mott insulators (parent high T_c and CMR compounds), has so far been unknown, but such information is crucial in understanding the fascinating Mott phenomena in a variety of condensed matter systems. With the availability of high brightness synchrotron facilities, a new frontier of understanding correlated systems would likely emerge.

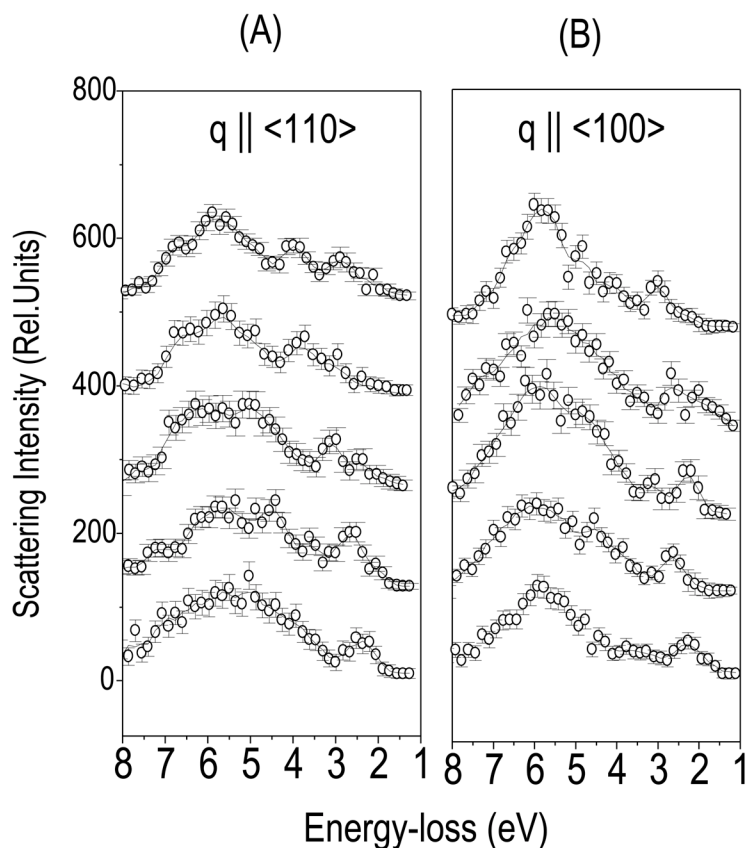


Figure 1: Inelastic x-ray scattering spectra near the Cu K-edge are shown along two directions in the Cu-O plane: (A) Scattering with \mathbf{q} along the $\langle 110 \rangle$ -direction (45 degrees to the Cu-O bond direction). (B) Scattering with \mathbf{q} along the $\langle 100 \rangle$ -direction (the Cu-O bond direction). Each curve (offset for clarity) represents a different $|\mathbf{q}|$ value.

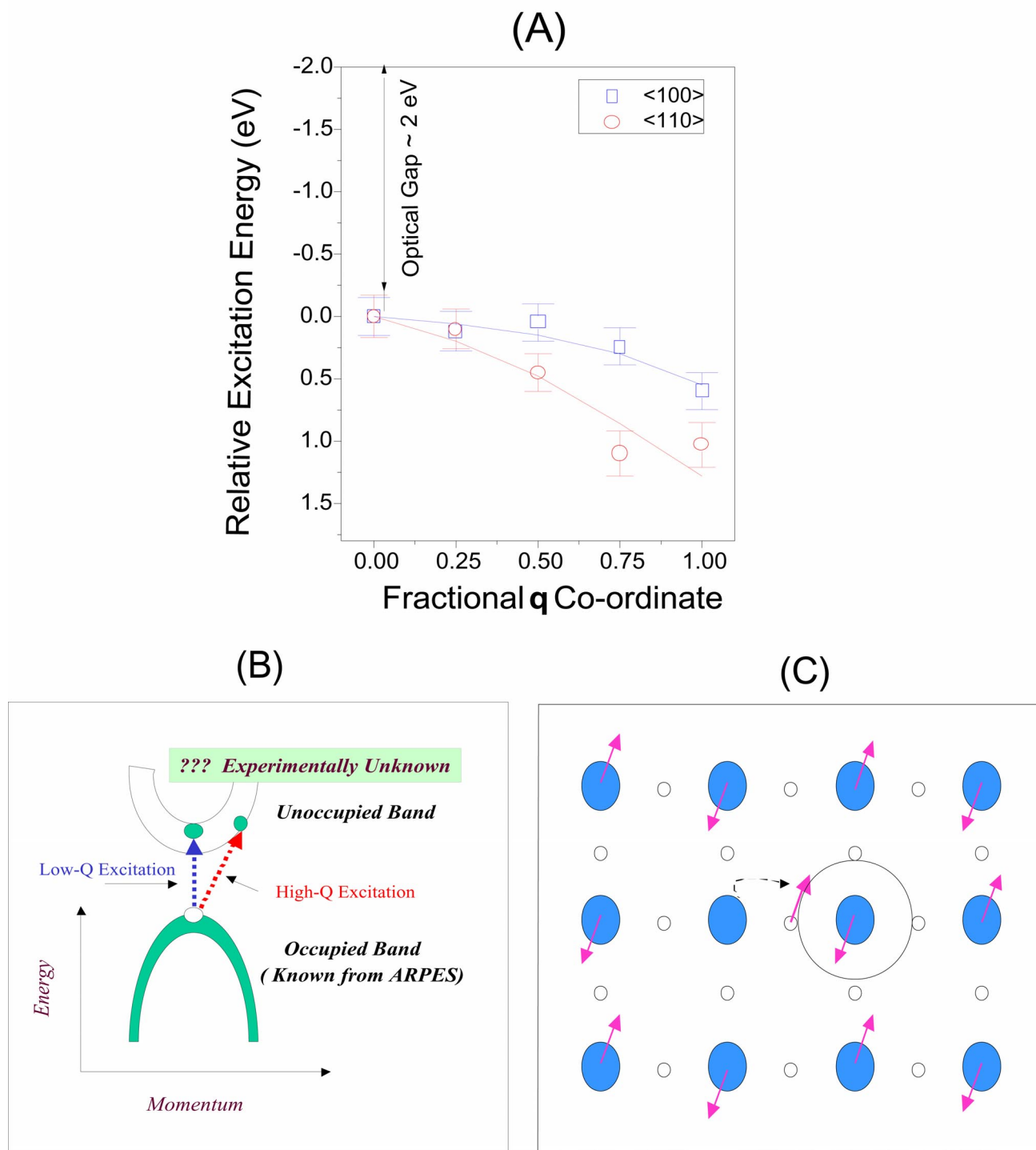


Figure 2: (A) Momentum dependence of the center of gravity of the low-energy inelastic feature is compared along the $\langle 110 \rangle$ and $\langle 100 \rangle$ directions. Relative excitation energies are plotted referenced to the energy (E_0) at $q = (0,0)$ along each direction. (B) Schematic cartoon of the possible energy gap in the electronic structure of the insulators, separating the occupied states from the unoccupied ones. A charge excitation gap exists between the occupied band and the unoccupied upper Hubbard band in cuprate insulators. The unique advantage of high-energy inelastic x-ray scattering is that it can probe charge excitations with finite momentum transfers over a large portion of the Brillouin zones. In insulating cuprates these excitations reveal the momentum structure of the upper Hubbard band. (C) Illustration of a particle-hole pair created in an antiferromagnetically ordered lattice.

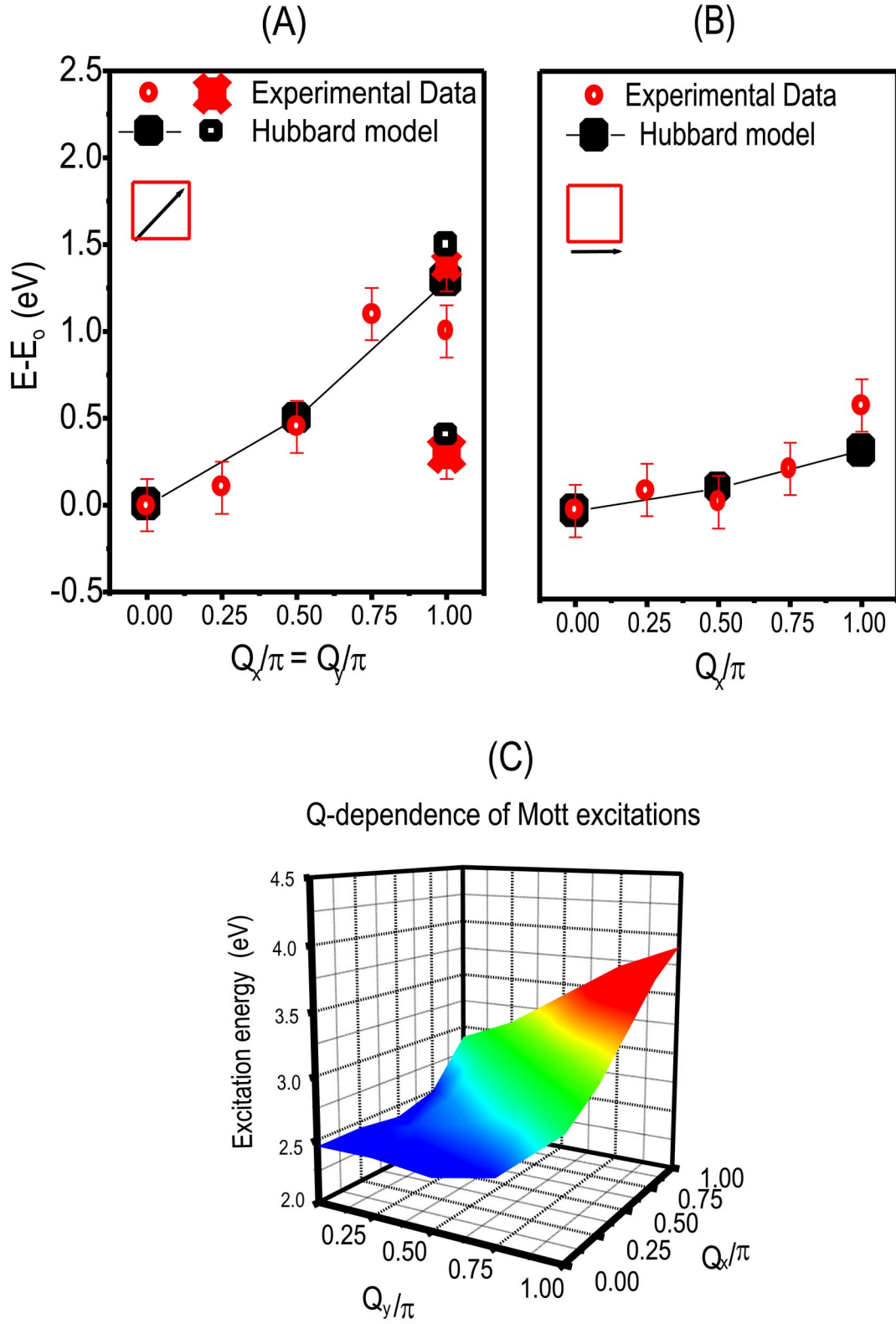


Figure 3: (A) and (B) A comparison of scattering results with numerical calculations based on the Hubbard model [11,12]. (C) A q -space map of the charge gap in parent high T_c cuprates, extracted from the IXS data.

We gratefully acknowledge P. Abbamonte and C. Kao for useful suggestions. This work was performed at the National Synchrotron Light Source of Brookhaven National Laboratory and was jointly supported by the Department of Energy (Materials Sciences Division) through the Stanford Synchrotron Radiation Lab of Stanford Linear Accelerator Center, Stanford, California and Bell Laboratories of Lucent Technologies, New Jersey.

References:

- [1] N. F. Mott Proc.Phys.Soc.London A **62**, 416 (1949).
- [2] J. Zaanen et.al., "Band gaps and electronic structure of transition-metal compounds" Phys. Rev. Lett. **55**, 418 (1985).
- [3] Z. X. Shen et.al., "Photoemission Studies of High T_c Superconductors: The Superconducting Gap" Science **267**, 343 (1995).
- [4] F. Ronning et. al., "Photoemission Evidence for a Remnant Fermi Surface and a d-Wave-like Dispersion in Insulating $\text{Ca}_2\text{CuO}_2\text{Cl}_2$ " Science **282**, 2067, (1998).
- [5] Y.Y.Wang et.al., "Momentum-Dependent Charge Transfer Excitations in $\text{Sr}_2\text{CuO}_2\text{Cl}_2$ Angle-Resolved Electron Energy Loss Spectroscopy" Phys. Rev. Lett. **77**, 1809 (1997).
- [6] F. Sette et.al., "Transition from Normal to Fast Sound in Liquid Water" Phys. Rev. Lett. **77**, 83 (1996).
- [7] C. C. Kao et.al., "X-ray resonant Raman scattering in NiO: Resonant enhancement of the charge-transfer excitations" Phys. Rev. B **54**, 16 361 (1996).
- [8] E. D. Isaacs et.al., "Inelastic x-ray scattering study of the metal-antiferromagnetic insulator transition in V_2O_3 " Phys. Rev. Lett. **76**, 4211 (1996).
- [9] J. P. Hill et. al. "Resonant Inelastic X-ray Scattering in Nd_2CuO_4 " Phys. Rev. Lett. **80**, 4967 (1998).
- [10] P. Abbamonte et.al., "Resonant Inelastic X-Ray Scattering from Valence Excitations in Insulating Copper Oxides" Phys. Rev. Lett. **83**, 860 (1999).
- [11] M. Z. Hasan et.al. "Electronic Structure of Mott Insulators Studied by Inelastic X-ray Scattering " et.al., Science **288**, 1811 (2000).
- [12] K. Tsutsui et.al., "Momentum Dependence of Resonant Inelastic X-Ray Scattering Spectrum in Insulating Cuprates" Phys. Rev. Lett. **83**, 3705 (1999).
- [13] S. L. Cooper et.al., "Optical Studies of a-, b- and c-axis charge dynamics $\text{YBa}_2\text{Cu}_3\text{O}_{(6+x)}$ " Phys. Rev. B **47**, 8233 (1993).
- [14] M. E. Simon et.al., "Excitons in Insulating Cuprates" Phys. Rev. B **54**, R3780 (1996).



Coupled capillary wave fluctuations in thin aqueous films on an aqueous subphase

M. Li, A. Tikhonov¹, M. Schlossman¹, and D. Chaiko²

¹University of Illinois at Chicago, ²Argonne National Laboratory

Wetting phenomena at interfaces are very sensitive to the form of the potential that governs the interaction between the interfaces. For example, x-ray scattering studies of thin wetting films on solid substrates have shown that thermal fluctuations of the liquid surface are reduced by the long-range van der Waals interaction from the substrate [1,2]. Studies of these thin films are useful for understanding the role of short and long-range forces in interfacial statistical physics; they also have a number of practical applications such as adhesion or lubrication.

We chose to study thin aqueous liquid films on top of bulk aqueous liquid substrates for several reasons. First, a major component of both the film and the substrate is water, with the other components chosen to be biologically compatible. Aqueous biphasic systems are used, for example, for the purification and separation of biological materials [3]. We anticipate that these thin films may be of use for biophysical studies and have already used them to study ordering in a protein monolayer at the liquid-liquid interface [4]. Second, the interfacial free energy potential that characterizes this

wetting phenomenon is between two liquid interfaces. Numerous x-ray scattering measurements have demonstrated the suitability of capillary wave theory to describe the fluctuations of a single liquid interface. When two liquid interfaces are placed in close proximity, the interfacial potential creates a coupling between the capillary fluctuations. We show that this coupling can be simply described by a perturbative modification of the capillary wave Hamiltonian. This allows us to determine the curvature near the minimum of the interfacial potential. By assuming a simple form for the interfacial potential we can also derive parameters that characterize the long- and short-range interactions between the interfaces.

The systems we studied are phase separated polyethylene glycol (PEG), potassium phosphate, and water mixtures[3]. The top phase is rich in PEG (denoted PEG*), and the bottom phase is rich in salt (salt*). The solutions were prepared by mixing $\text{K}_2\text{HPO}_4/\text{KH}_2\text{PO}_4$ (from Fluka, 99.5%, ratio yielding pH 7.9), PEG (from Aldrich, $M_n=3400$), and Barnstead Nanopure water. The mixtures were shaken thoroughly and allowed to equilibrate.

brate for more than 20 hours at room temperature. The two phases were then extracted separately. The interfacial tension between the two phases and the surface tensions of each phase with its vapor were measured by the drop-weight [5] and Wilhelmy plate methods, respectively [6] (Table I).

X-ray reflectivity and diffuse scattering measurements were performed on beamline X19C at the NSLS, as described elsewhere [7]. A vapor-tight Teflon sample cell with a circular trough for the liquid sample and a water reservoir to maintain the humidity was temperature controlled to $\pm 0.003^\circ\text{C}$. The sample was prepared by placing a small drop of the top phase onto the bottom phase surface. The drop spreads and thins rapidly, as is evident from the rapidly changing optical interference pattern that spreads across the surface. After a few seconds the thin layer becomes unstable and forms an irregular pattern, which then collapses to form small lenses in about one hour. A pipette is used to mechanically move the lenses out of the x-ray beam path. The macroscopic lenses function as reservoirs for the partially wet PEG* top phase. The following re-

sults are independent of the precise volume of the initial small drop.

Figure 1 (open circles) shows an example of the specular reflectivity normalized by the Fresnel reflectivity as a function of the wave vector transfer Q_z (for specular reflection $\beta=\alpha$, $Q_x=Q_y=0$, and $Q_z=(4\pi/\lambda)\sin\alpha$, where $\lambda=0.825\text{ \AA}$). The decay of the oscillations in the normalized reflectivity can be modeled by the presence of different interfacial widths at the liquid-vapor and liquid-liquid interfaces. The solid curve shown in Figure 1 is a fit from a standard analysis of the reflectivity using the Born approximation with a single slab model [7,8]. This analysis yields the layer thickness $l_m=42.1\text{ \AA}$, the interfacial width, and the electron density of the film relative to the subphase (Table I). The liquid-liquid interfacial width is much greater than the liquid-vapor width because the liquid-liquid interfacial tension is much less (Table I). Our measurements indicate that the layer is a thin film of a PEG-rich solution rather than just a monolayer of PEG molecules adsorbed to the interface. Previous measurements have shown that a monolayer would have a thickness of 10 \AA , less than the thickness of our film [9]. Also, the radius of gyration of our PEG under similar conditions has been measured to be close to 10 \AA , also less than the film thickness [10]. Figure 1 also shows the background scattering intensities (solid circles) measured by offsetting in Q_y from the specular condition [7]. Oscillations in the background scattering mimic those in R/R_F , indicating that the capillary wave fluctuations between the two interfaces are in phase to some extent [11,12].

To further probe the coupling of the capillary wave fluctuations between the two interfaces, we measured diffuse scattering from the interfaces by scanning β for fixed $\alpha=0.56\text{ deg}$ and $\alpha=0.75\text{ deg}$, as shown in Figure 2. Diffuse scattering data from single liquid interfaces roughened by thermal capillary wave fluctuations have been previously described by the distorted wave Born approximation [12,13]. The interfacial roughness is characterized by the height-height correlation function, defined as $C(\mathbf{r})=\langle\zeta(0)\zeta(\mathbf{r})\rangle$, where $\zeta(\mathbf{r})$ is the local interfacial height above the mean interfacial plane, and \mathbf{r} is the displacement between two points on the interface. This correlation function is determined by an analysis of the capillary wave Hamiltonian. Here, we modify the standard capillary wave Hamiltonian to account for the interfacial coupling, derive the correlation functions,

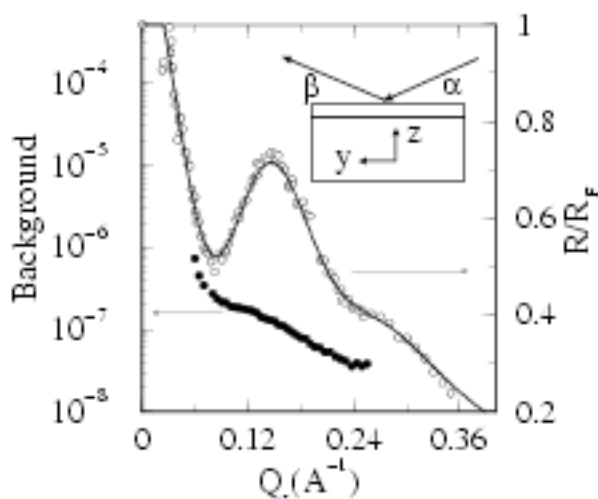


Figure 1. specular reflectivity intensity normalized to the Fresnel reflectivity, R/R_F (open circles). Fit described in the text. Off-specular background scattering intensities (solid circles). Inset: This aqueous layer on top of an aqueous subphase illustrated with the geometry of x-ray scattering.

Table I									
Sample parameters measured. Overall concentration is given (top phase is 60% PEG, 0.3% salt, 39.7% water; bottom phase is 3.5% PEG, 38.4% salt, 58.1% water). Symbols are defined in the text.									
c(wt%)		$\gamma_{\text{interface}}$ (mN/m)			$\rho_{\text{e, film}}/\rho_{\text{e, sub}}$		l_m	B	σ_1
PEG	salt	PEG*/air	salt*/air	PEG*/salt*			(\AA)	(J/m^4)	(\AA)
13.2 ± 0.1	28.9 ± 0.1	51.6 ± 0.5	77.2 ± 0.5	7 ± 1	0.84 ± 0.02		42.1 ± 0.3	$1.4(+1.6/-0.8) \times 10^{11}$	3.2 ± 0.2
									8.3 ± 0.3

and compute the diffuse scattering from the distorted wave Born approximation.

Our modification of the Hamiltonian proceeds from the observation that the equilibrium thickness of the film corresponds to a minimum in the interfacial potential, or excess free energy of the wetting film, ΔG . This occurs at the point l_m (see Figure 3) at which $\partial\Delta G/\partial l=0$. We expand $\Delta G(l)$ near the minimum to second order, $\Delta G(l)=C+0.5B(l-l_m)^2$, to get the coupling constant B between the two interfaces. Adding the energy of the thermal fluctuations to the free energy [16,17], one has the Hamiltonian of the system, per unit area [15,17,18], (see Equation 1) where A_0 is the interfacial area, $i=1,2$ refers to the PEG*-air interface and salt*-air interface, respectively, ζ_{ix} is the x-derivative of ζ_i , γ_i is the interfacial tension, g is the gravitational acceleration, and $\Delta\rho_{mi}$ is the difference in mass density across interface i . The upper equation is the standard capillary wave Hamiltonian [14] with the addition of the term proportional to B that represents a local coupling of the positions of the two interfaces. The lower equation is a representation in reciprocal space, where $\alpha(q)$ is the Fourier transform of $\zeta(\mathbf{r})$ with \mathbf{q} being the in-plane capillary wave vector. The canonical average of the correlation functions in reciprocal space is given by (See Equation 2) where k_B is Boltzmann's constant, T is the temperature, and $M_i=B/2+g\Delta\rho_{mi}/2+\gamma_i q^2/2$, $i=1,2$. The Fourier transforms of Equations (2) are the height-height correlation functions of the individual interfaces, $C_{11}(\mathbf{r})$, $C_{22}(\mathbf{r})$, and the height-height cross-correlation function between the two interfaces, $C_{12}(\mathbf{r})$.

The distorted wave Born approximation for x-ray scattering from one interface [2,13] can be modified for our two interface geometry to yield the intensity of diffuse scattering (see Equation 3), where I_0 is incident intensity, Q_c is the wave vector for total reflection, $T(\alpha)$ and $T(\beta)$ are the Fresnel transmission coefficients, $\Delta\rho_i$ is the difference in electron density across each interface, Q_z^i is the z-component of the momentum transfer with respect to the lower phase, and σ_i is the roughness of each interface. Integration over β and ϕ corresponds to the angular acceptance range of the x-ray instrument (resolution volume) determined by the detector slits (0.4 mm vertical by 10 mm horizontal).

The data at both incident angles in Figure 2 are fit using Eq. (3) combined with the standard expression for the reflectivity from the distorted wave Born approximation [13]. Two parameters are fit, the coupling B and a small constant background that represents scattering from the bulk. The analysis yields $B=1.4(+1.6/-0.8)\times 10^{11}\text{J/m}^4$ and is shown by the solid lines in Fig. 2.

It is interesting to compare our measured coupling constant B to a coupling constant B_H previously derived for interacting tensionless membranes whose fluctuations are determined by the membrane's bending modulus κ rather than the interfacial tension as in our system. The Helfrich Hamiltonian leads to $B_H=36k_B T^2/(\pi^2\kappa l^4)$, which yields $B_H=1.2\times 10^{12}\text{J/m}^4$ for flexible membranes with $\kappa\sim k_B T$ or $B_H=2.8\times 10^{10}\text{J/m}^4$ for a rigid liquid crystalline membrane with $\kappa\sim 40k_B T$ [19]. The coupling in our system lies sensibly between these values for the coupling within a stack of either flexible or rigid ten-

$$H = \frac{1}{A_0} \int d^2r \left\{ \sum_{i=1,2} \left[\gamma_i \left(1 + \frac{1}{2} \zeta_{ix}^2 + \frac{1}{2} \zeta_{iy}^2 \right) + \frac{1}{2} g \Delta\rho_{mi} \zeta_i^2 \right] + \frac{1}{2} B (\zeta_1 - \zeta_2)^2 \right\} \quad (1)$$

$$= \sum_{i=1,2} \left\{ \gamma_i + \sum_q \frac{1}{2} (B + g \Delta\rho_{mi} + \gamma_i q^2) \alpha_i(q) \alpha_i(-q) \right\} - \frac{1}{2} B \sum_q [\alpha_1(q) \alpha_2(-q) + \alpha_1(-q) \alpha_2(q)]$$

$$\langle \alpha_1(q) \alpha_1(-q) \rangle = \frac{2}{A_0} \frac{k_B T M_2}{4 M_1 M_2 - B^2} ; \langle \alpha_2(q) \alpha_2(-q) \rangle = \frac{2}{A_0} \frac{k_B T M_1}{4 M_1 M_2 - B^2} ; \langle \alpha_1(q) \alpha_2(-q) \rangle = \frac{2}{A_0} \frac{k_B T B}{4 M_1 M_2 - B^2} \quad (2)$$

$$I_{diff} = \frac{I_0}{\sin \alpha} \frac{Q_c^4}{256\pi^2} \int d\beta d\phi |T(\alpha)|^2 |T(\beta)|^2 \left\{ \sum_{j=1,2} \left[\Delta\rho_j^2 \frac{e^{-\sigma_j^2 \text{Re}(Q_z^j)^2}}{|Q_z^j|^2} \int (e^{|Q_z^j|^2 C_{jj}(r)} - 1) e^{iQ_{xy}r} d^2r \right] + \right. \\ \left. 2\Delta\rho_1 \Delta\rho_2 \cos(Q_z l_m) \frac{e^{-\frac{1}{2}(\sigma_1^2 + \sigma_2^2) \text{Re}(Q_z^j)^2}}{|Q_z^j|^2} \int (e^{|Q_z^j|^2 C_{12}(r)} - 1) e^{iQ_{xy}r} d^2r \right\} \quad (3)$$

sionless membranes. Our measurement of B can also be compared to a compression modulus measured for freely suspended soap films, B_{soap} , that span the range from 10^{11} J/m^4 to 10^{14} J/m^4 , depending upon composition [20]. This indicates that the coupling of interfacial fluctuations in soap films is either similar to or greater than in our thin film. A simple model for the free energy F (per unit area) of this film of thickness l is $F(l) = \gamma_{\text{salt}^*/\text{PEG}^*} + \gamma_{\text{PEG}^*/\text{air}} + \Delta G(l)$ [21]. For large l , $\Delta G(l)$ tends to zero. The interfacial potential $\Delta G(l)$ includes a repulsive short-range force and an attractive long-range van der Waals interaction, written as (See Equation 4) [22–24] where S_p is the amplitude of the short-range interaction, A is an effective Hamaker constant, and l_0 sets the distance for the hard core (Born) repulsion [23,24]. The first term in Eq. (4) models a short-range interaction with decay length L , and the second term is the van der Waals interaction between two planar interfaces separated by a distance l . It has been shown that this model can account for many features of wetting films, including the pseudo partial wetting that occurs in our system [21,22].

Using the literature value of $l_0 = 1.57 \text{ \AA}$ [23], the other three parameters in Eq. (4) can be determined by the following conditions. (1) $\Delta G(l \rightarrow l_0) = S$, where the spreading coefficient $S = \gamma_{\text{salt}^*/\text{air}} - (\gamma_{\text{salt}^*/\text{PEG}^*} + \gamma_{\text{PEG}^*/\text{air}}) = 18.6 \text{ mN/m}$ is given by our macroscopic measurements of the tensions [21]. (2) At the minimum of the interfacial poten-

tial, $\partial \Delta G(l_m) / \partial l = 0$ and $\partial^2 \Delta G(l_m) / \partial l^2 = B$, where l_m is given by the fit to the reflectivity data, and B is given by the fit to the diffuse scattering data. These conditions yield $\Lambda = 2.9 \pm 0.2 \text{ \AA}$, $S_p = 18.7 \pm 0.1 \text{ mN/m}$, and $A = 8(+10/-5) \times 10^{-23} \text{ J}$. The excess free energy given by Eq. 4 with these parameters is plotted in Figure 3. The decay length L is similar to the close-packed distances of these molecules, though the origin of the short-range interaction is not well understood [25]. The sign of the Hamaker constant and the spreading coefficient are consistent with our observation of pseudo partial wetting in which small drops are in equilibrium with a very thin layer that covers the interface (see inset in Figure 3) [21]. The effective Hamaker constant is the difference between two Hamaker constants, $A = A_{\text{PEG}^*, \text{PEG}^*} - A_{\text{PEG}^*, \text{salt}^*}$. A is small ($A \sim k_B T / 50$), indicating that the attraction of the upper phase for the lower phase is only slightly different from the attraction of the upper phase to itself.

We have formed nanometer-thick aqueous films supported on an aqueous subphase and have shown that x-ray scattering can be used to probe coupled interfacial fluctuations in these thin films. A perturbative, local modification of the standard capillary wave Hamiltonian allowed us to determine a coupling constant for these interfaces. Combining the x-ray measurements with macroscopic measurements of the interfacial tensions allowed us to determine the parameters in a model free energy for the thin film. These included the

$$\Delta G(l) = S_p e^{(l_0 - l)/\Lambda} - A / 12\pi l^2 \quad (4)$$

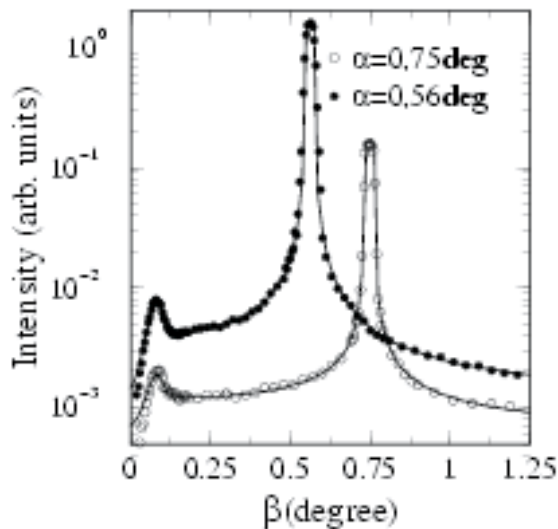


Figure 2. Off-specular diffuse scattering at $\alpha = 0.56 \text{ deg}$ (dots) and $\alpha = 0.75 \text{ deg}$ (circles). Fit described in the text.

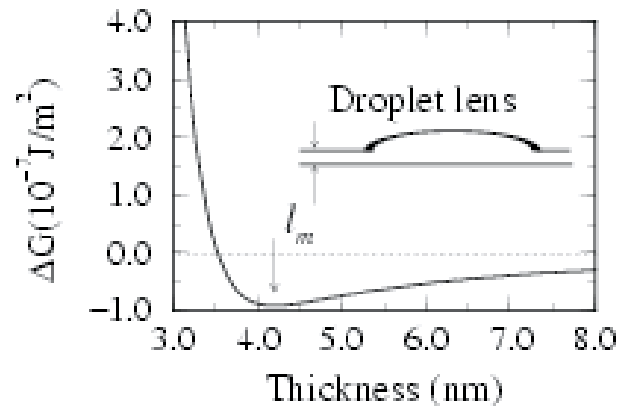


Figure 3. Interfacial potential, $\Delta G(l)$, given in Eq.(4) with parameters given in the text. Inset: Macroscopic lens in equilibrium with a film of thickness l_m (not to scale).

Hamaker constant describing the long-range interactions and the decay length and amplitude of the short-range interactions.

References:

- [1] I.M. Tidswell, T.A. Rabedeau, P.S. Pershan, and S. D.Kosovsky, Phys. Rev. Lett. 66, 2108 (1991).
- [2] A.K. Doerr, et al., Phys. Rev. Lett. 83, 3470 (1999); J. Wang et al., Phys. Rev. Lett. 83, 564 (1999).
- [3] B.Y. Zaslavsky, Aqueous Two-Phase Partitioning (Marcel Dekker, New York, 1995); P.A. Albertsson, Partition of Cell Particles and Macromolecules (Wiley, New York, 1986).
- [4] M. Li, A.M. Tikhonov, D.J. Chaiko, and M.L. Schlossman, to be published.
- [5] J.L. Lando and H.T. Oakley, J. Colloid Interface Sci. 25, 526 (1967).
- [6] A.W. Adamson, Physical Chemistry of Surfaces (Wiley, New York, 1992).
- [7] M.L. Schlossman, D. Synal, Y. Guan, et al., Rev. Sci. Instru. 68, 4372 (1997).
- [8] M.L. Schlossman and P.S. Pershan, in Light Scattering by Liquid Surfaces and Complementary Techniques, ed. D. Langevin (Marcel Dekker, New York, 1992), p. 365.
- [9] J.A. Benderson, R. Richards, J. Penfold, R. Thomas, and J.R. Lu, Macromolecules, 26, 4591 (1993).
- [10] P. Thiagarajan, D.J. Chaiko, and R.P. Hjelm, Macromolecules 28, 7730 (1995).
- [11] S. Garoff, E.B. Sirota, S.K. Sinha, and H.B. Stanley, J. Chem. Phys. 90, 7505 (1989).
- [12] D.K. Schwartz, M.L. Schlossman, E.H. Kawamoto, et al. Phys. Rev. A 41, 5687 (1990).
- [13] S.K. Sinha, E.B. Sirota, S. Garoff, and H.B. Stanley, Phys. Rev. B 38, 2297 (1988).
- [14] B.V. Derjaguin, N.V. Churaev, and V.M. Muller, Surface Forces (Consultants Bureau, New York, 1987).
- [15] M.O. Robbins et al. Phys. Rev. A 43, 4344 (1991); D. Andelman, et al. Europhys. Lett. 7, 731 (1988).
- [16] J.S. Rowlinson and B. Widom, Molecular Theory of Capillarity (Clarendon Press, Oxford, 1982).
- [17] M.L. Schlossman, M. Li, D. and A. Tikhonov, in Applications of Synchrotron Radiation Techniques to Materials Science V, eds. S.R. Stock, S.M. Mini, D.L. Perry (Mat. Res. Soc., Warrendale, PA, 2000), p. 165.
- [18] F.P. Buff, R.A. Lovett, and F.H. Stillinger, Phys. Rev. Lett. 15, 621 (1965).
- [19] W. Helfrich, Z. Naturforsch. 33a, 305 (1978).
- [20] S.A. Safran, Statistical Thermodynamics of Surfaces, Interfaces, and Membranes (Addison Wesley, Reading, MA, 1994).
- [21] J. Daillant and O. Belorgey, J. Chem. Phys. 97, 5837 (1992).
- [22] A. Sharma and R. Khanna, Phys. Rev. Lett. 81, 3463 (1998).
- [23] C.J. van Oss, Interfacial Forces in Aqueous Media (Marcel Dekker, New York, 1994).
- [24] J. Israelachvili, Intermolecular and Surface Forces (Academic Press, London, 1991).
- [25] P.G. de Gennes, Rev. Mod. Phys. 57, 827 (1985); F. Brochard-Wyart, et al. Langmuir 7, 335 (1991).
- [26] T. Pfohl and H. Rieger, Phys. Rev. Lett. 82, 783 (1999).



Application of Polarization Modulation in the Study of Magnetic Thin Film, Multilayers and Interfaces

C. Sánchez-Hanke¹, D. Lott¹, C.-C. Kao¹, J.B. Hastings¹, S.L. Hulbert¹, E.D. Johnson¹, J.C. Sutherland², D. Monteleone², and J. Trunk².

¹National Synchrotron Light Source, Brookhaven National Laboratory, Upton, New York

²Biology Department, Brookhaven National Laboratory, Upton, New York

Over the past decade, many new synchrotron based experimental techniques have been developed for the study of magnetism and magnetic materials [1]. In particular, x-ray magnetic circular dichroism (MCD), the difference in the absorption coefficient between left and right polarized x-rays for a magnetized sample, has become a powerful tool for the characterization of many technologically important magnetic materials. The major advantages of MCD, in comparison with standard magnetic measurements such as SQUID, VSM or MOKE, are element specificity, very large MCD effects, and the orbital and spin sum rules. Furthermore,

the x-ray MCD effect can be measured in circularly polarized x-ray specular reflectivity and diffuse scattering modes to provide information on magnetization density profile and magnetic interface roughness of the sample.

Up to now, a typical x-ray MCD measurement keeps the x-ray polarization constant while the sample magnetization is reversed, thus reducing systematic errors that can occur in MCD measurements. However, there are many situations where polarization modulation is desirable, for example, in the study of samples requiring very high magnetic fields and samples with very

small MCD effects. Polarization modulation is a technique commonly used in synchrotron UV natural circular dichroism (CD) measurements to extract a small CD signal from a large background [2]. However, only recently have the necessary x-ray optical elements, such as diamond phase retarding plates and special insertion devices capable of polarization switching, become available for performing polarization modulation measurements in both the soft and hard x-ray regions.

Recently, we have implemented a phase-sensitive detection scheme based on polarization modulation from the Elliptically Polarized Wiggler located in the X13 straight section of the NSLS x-ray ring [3]. The EPW provides elliptically polarized x-rays, and the polarization of the x-rays can be switched with frequencies up to 100 Hz. Our experiment uses switching frequencies of 2 Hz and 22 Hz. The radiation from the EPW feeds a soft-x-ray beamline, X13A, and a hard-x-ray beamline, X13B. Figure 1 shows the phase-sensitive detection scheme as well as the application of this technique to measure element specific hysteresis loops. As indicated in the center panel of Figure 1, two lock-in amplifiers are used for the measurement. The first lock-in is set to the wiggler switching frequency (f) to detect the difference signal ($\Delta I = I_{\uparrow\uparrow} - I_{\downarrow\uparrow}$), where the first arrow represents the polarization of the x-ray and the second arrow the sample magnetization direction. The second lock-in is set to twice the wiggler switching frequency ($2f$) and measures the sum signal ($I = I_{\uparrow\uparrow} + I_{\downarrow\uparrow}$). In ad-

dition, a chopper is used to block the linearly polarized transients from the EPW. With this detection scheme, the MCD effect is simply the difference of these two lock-in signals, and magnetic field dependent measurements can be performed in a straightforward manner. The upper left of Figure 1 shows a typical MCD and absorption spectra, while an element sensitive hysteresis loop is shown in the upper right. In this measurement, the incident energy is selected close to the absorption edge of one of the elements contained in the sample where the MCD effect is maximized. The hysteresis loop is then obtained by recording the MCD signal as a function of applied magnetic field.

The sensitivity of the MCD polarization modulation technique is demonstrated in a study of the following example system: a $[\text{Co}_{90}\text{Fe}_{10}(10\text{\AA})/\text{Cu}(13\text{\AA})]_{20}$ giant magnetoresistance (GMR) multilayer grown on Si [4]. Since the GMR effect is found to be very sensitive to the interface between the ferromagnetic layer and the non-magnetic spacer, there has been a great deal of interest in understanding the magnetic properties of the interface, such as magnetic roughness and induced moment. Figure 2 shows the hysteresis loops measured at the L_3 absorption edges of Fe (707 eV), Co (778 eV), and Cu (932.5 eV), respectively. In this case, specular reflectivity was measured, and the asymmetry ratio, defined as $\Delta I / I$, is plotted. The EPW switching frequency was set to 22 Hz. For Fe and Co, roughly 2% and 15% asymmetry ratios are observed, while for Cu, the asymmetry ratios due to the induced moments

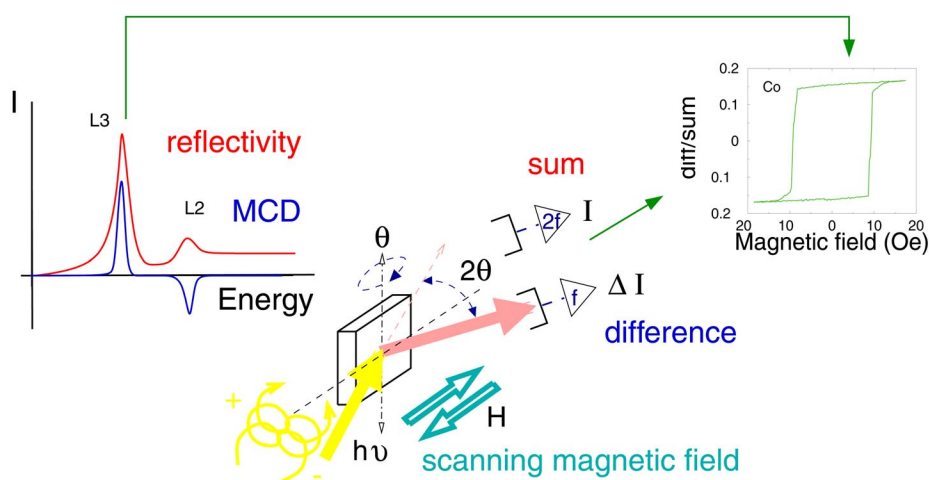


Figure 1: Schematic of polarization modulation detection and its application to MCD and element sensitive hysteresis loop measurements.

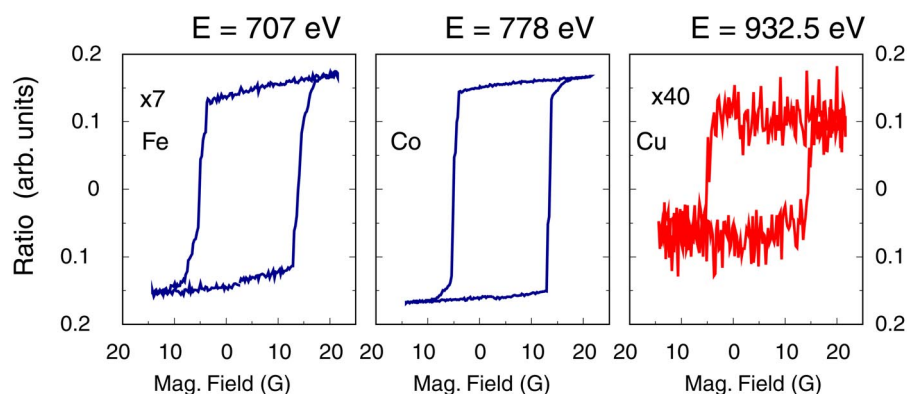


Figure 2: Element sensitive hysteresis loops recorded from a $[\text{Co}_{90}\text{Fe}_{10}(10\text{\AA})/\text{Cu}(13\text{\AA})]_{20}$ multilayer.

are on the order of 10^{-3} . It should be noted that in specular reflectivity mode, the asymmetry ratios are a strong function of the scattering angle. Previous MCD measurements on a series of Co/Cu multilayers have estimated that, for this particular Cu spacer thickness, the induced moment on Cu is only $0.013 \mu_B$ (where $\mu_B \equiv eh/2m_e$ is a Bohr magneton) [5]. The clear observation of the Cu induced moment demonstrates the ability of polarization modulation to improve the sensitivity of an MCD measurement.

The application of polarization modulation to a magnetic field dependent measurement is demonstrated in the study of a Co/NiO exchange biased sample [6]. Exchange bias refers to a shift of the hysteresis loop of a magnetic system from zero along the applied magnetic field axis due to the presence of ferromagnetic/antiferromagnetic interfaces. It is an important ingredient in the design of spin-valve structures for magnetic recording applications. The central issue in a quantitative understanding of this phenomenon is, again, the interfacial magnetic properties. Furthermore, it is essential in this case to characterize the interface as a function of applied magnetic field, since it is the difference in the interface magnetic properties as a function of applied field that is responsible for the observed exchange bias field. Figure 3 shows the element specific hysteresis loops measured at the L3 absorption edge of Co (left) and Ni (right). The asymmetry ratios are shown for a measurement carried out in specular reflectivity mode at a 10° incident angle.

In order to present both loops on the same scale, the Ni loop has been scaled by a factor of 35 and shifted to center the Ni loop along the magnetization axis. The presence of the Ni MCD effect indicates the existence

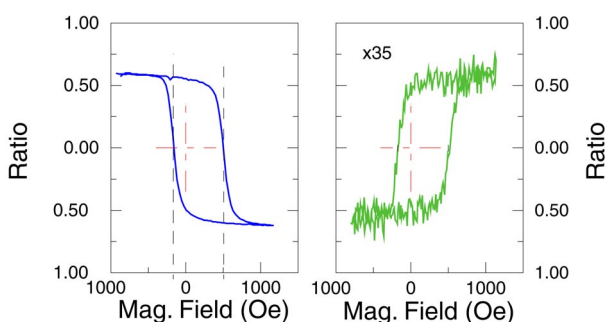


Figure 3: Element sensitive hysteresis loops recorded from a Co (3nm)/ NiO (50nm) exchange bilayer.

of uncompensated Ni spins within the structure, while the presence of the hysteresis loop shows that a certain amount of the uncompensated spins are not bound to the antiferromagnetic lattice and are switching along with the ferromagnetic layer. It is also important to note that the orientation of the two hysteresis loops are opposite to each other, suggesting that the observed Ni spins are antiferromagnetically coupled to the Co. Finally, angular dependence in specular reflectivity measured at the two saturation states of the hysteresis loop (not shown here) reveals a difference in the effective ferromagnetic Ni thickness. This example clearly demonstrates the unique information, which can be provided by polarization modulation technique.

Both measurements illustrated here explore the large MCD effects that can be found in the soft-x-ray region. The strong resonant scattering amplitude or absorption limits the technique to thin samples. Although K-edge MCD effects from transition metals are

roughly two orders of magnitude smaller than those at the L-edges, these very small MCD effects can still be used effectively with polarization modulation. Figure 4 shows the specular reflectivity as well as the asymmetry ratios measured at the Fe K-edge from an exchange biased multilayer system: $[\text{Fe } 50\text{\AA} / \text{Cr } 20\text{\AA}]_4^{\text{FM}} / [\text{Fe } 14.5\text{\AA} / \text{Cr } 11.5\text{\AA}]_{19}^{\text{AFM}} / \text{Cr } 200\text{\AA} / \text{MgO substrate}$ [7]. The sample consists of a ferromagnetic Fe/Cr multilayer and an antiferromagnetic multilayer. The data clearly show that it is possible to observe magnetic scattering in these systems even though the MCD effect at the Fe K-edge is only $\sim 10^{-3}$. In this case, charge reflectivity was used to fit the layer thickness and interfacial roughness. These parameters are then used in the fitting of the magnetization density profile of the whole multilayer. The solid line in the lower panel of Figure 4 is the simulation result for the proposed magnetic structure [8].

Acknowledgements

Work done at the National Synchrotron Light Source was supported by DOE, under contract No. DE-AC02-76CH00016.

References

1. For example, S.W. Lovesey, S.P Collins, "X-ray Scattering and Absorption by Magnetic Materials", Oxford University Press (1996).
2. For example, see J. C. Sutherland, chapter in "Circular Dichroism and the Conformational Analysis of Biomolecules", edited by G.D. Fasman, pp 599-633. New York: Plenum Press (1996); B.A. Wallace, J. Synchrotron Rad., 7, 289-295 (2000).
3. J.C. Sutherland, K. Polewski, D. Monteleone, J. Trunk, C. Sánchez-Hanke, S. L. Hulbert, C-C. Kao and E. D. Johnson, submitted to Rev. Scientific Instruments.
4. C. Sánchez-Hanke, C-C. Kao, J. B. Hastings, S. L. Hulbert, E. D. Johnson, J. C. Sutherland, D. Monteleone and J. Trunk, in preparation.
5. M. G. Samant, J. Stöhr, S. S. Parkin, G. A. Hekd, B. D. Hermesmeier, F. Hernan, M. van Schilfgaarde, L.-C. Duda, d. C. Mancini, N. Wassdahl, and R. Nakajima, Phys. Rev. Lett. 72, 1112 (1994).
6. C. Sánchez-Hanke, and C-C. Kao, to be published in J. Magn. Mater.
7. S. G. E. te Velhuis, G. P. Felcher, J. S. Jiang, A. Inomata, C. S. Nelson, A. Berger, and S. D. Bader, Appl. Phys. Lett. 75, 4174 (1999).
8. D. Lott et al, in preparation.

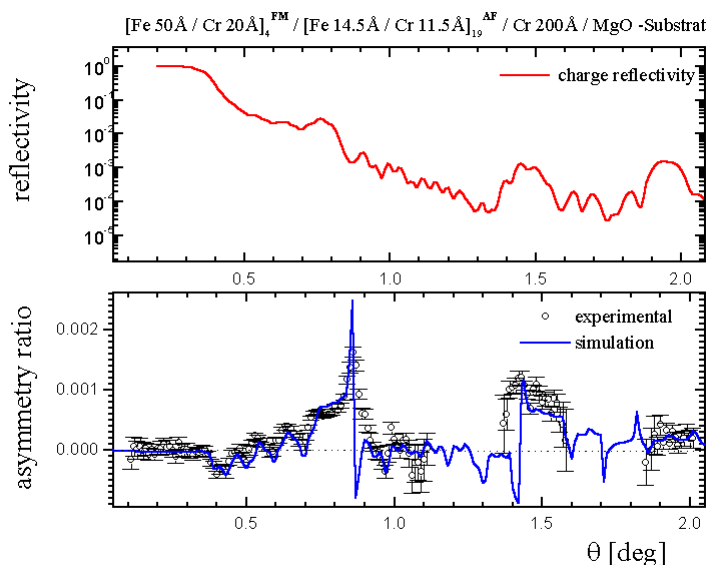


Figure 4: specular reflectivity and asymmetry ratios measured at Fe K-edge from an exchange biased multilayer system: $[\text{Fe } 50\text{\AA} / \text{Cr } 20\text{\AA}]_4^{\text{FM}} / [\text{Fe } 14.5\text{\AA} / \text{Cr } 11.5\text{\AA}]_{19}^{\text{AFM}} / \text{Cr } 200\text{\AA} / \text{MgO substrate}$

When Solids Run

D. E. Silva¹, P. E. Sokol¹, D. W. Brown^{1,2}, S. N. Ehrlich³

¹Department of Physics, The Pennsylvania State University

²Los Alamos Neutron Scattering Center, Los Alamos National Laboratory

³National Synchrotron Light Source, Brookhaven National Laboratory

Porous materials are playing an increasingly important role as a fertile playground for the exploration of fundamental scientific issues and diverse technological applications. Surface interactions and finite size effects play a key role in the qualitative modification of the properties of the materials contained within the porous host. On the practical level, such systems are of great importance in a variety of situations, ranging from adhesion, catalysis, lubrication, tribology and the engineering of materials. At the fundamental level, the nature of the phases and their transitions are qualitatively different from the bulk.

Microscopic structural studies of materials confined to mesoporous media have only recently been undertaken. Porous glasses, such as Vycor, have been a popular medium for studies of confined solids, since they are easily produced in a variety of pore sizes and have rigid structures. In some cases, such as Hg in Vycor¹, the structure of the confined solid is identical to that of the bulk, while in other cases, such as H₂O and D₂ in Vycor^{2,3}, confinement stabilizes new structures not present in the bulk. Confinement can even suppress crystalline order, such as O₂ in xerogel⁴. Recent X-ray diffraction studies of Ar and Kr adsorbed in porous glasses, carried out on the MATRIX beamline (X18A) at the NSLS, showed a hitherto unobserved behavior – the introduction of a new solid-solid phase transition due to disorder⁵.

The scattering from Ar in Vycor is shown in Figure 1. As in many other systems, the structure of the liquid phase (T=85K) is quite similar to that of the bulk liquid. Solidification, as marked by the appearance of diffraction peaks, does not occur until 64.5K, much lower than the bulk melting temperature of 84K. The structure of the high T solid phase (T=55K) is not the FCC bulk structure. Instead, the confined solid forms a disordered hexagonal close packed (DHCP) struc-

ture, characterized by random plane stacking. This structure arises from the disruption of the normal ABC stacking responsible for the FCC phase by the maximal number of stacking faults. Such structures have been observed in other close packed systems, such as D₂ in Vycor³, which is HCP in the bulk but forms a DHCP structure when confined.

Upon further cooling, a new phase transition is observed, as can be seen from the appearance of very sharp diffraction peaks (T=37K in Fig. 1). This new transition was totally unexpected since no comparable transition occurs in the bulk. While disorder has been known to suppress solid-solid phase transitions⁶, we believe that this is the first occurrence of a disorder introduced solid-solid phase transition. This structural transition is repeatable on cycling and appears to be a true thermodynamic phase, rather than a metastable one.

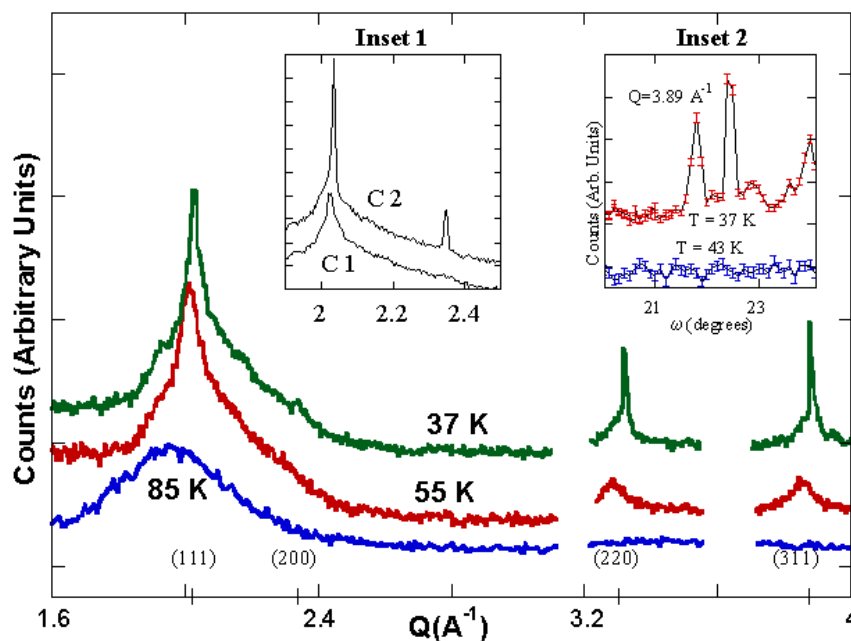


Figure 1: Diffraction measurements of Ar in Vycor at 85K, 55K, and 37K with the background subtracted. Inset 1 shows the diffraction pattern in the low temperature phase from consecutive cooling cycles (C1 and C2). Note the difference in intensity of the (111) and (200) peaks between cycles. Inset 2 shows a rocking curve with the detector fixed on the (311) peak for the high T solid (43K) and low T solid (37K). (adapted from Brown, et. al⁵)

The new phase can be easily identified by the appearance of sharp (resolution limited) diffraction peaks. Inset 1 of Figure 1 shows two different thermal cycles that show the appearance of two different sets of peaks in the low temperature solid. Cycle 1 appears to remain DHCP, as evidenced by the relatively broad (111) peak. However, cycle 2 is quite different in that a sharp peak forms atop the (111) reflection. With the appearance of the (200) reflection, this new structure is consistent with FCC. The nature of this new phase can be understood by examining the peak intensity while reorienting the sample (rocking curve), as shown in Inset 2. In the high temperature phase ($T=43\text{K}$), there is no variation in the intensity of the (311) peak, as expected for a random powder. However, in the low temperature phase ($T=37\text{K}$), there is a pronounced variation, indicating that the low temperature phase is a coexistence of a DHCP powder, with a correlation length comparable to the pore size, and large FCC crystallites that span many pores.

To further elucidate the nature of this transition, we have recently carried out diffraction measurements on Ar confined in Britesorb⁰⁷, a commercial sol-gel glass. This glass has a different morphology than Vycor, as well as a slightly larger pore size and higher porosity. Still, the glasses are quite similar and we would expect that they should show similar behavior (i.e. a DHCP solid at high temperature and a new solid phase at lower temperatures). The scattering from Ar in this sol-gel glass, shown in Figure 2, quickly shows that this is not the case.

As in the studies of Vycor, the liquid structure ($T=84\text{K}$) is similar to that in the bulk. A DHCP structure ($T=60\text{K}$) is observed on freezing at a temperature below the bulk freezing temperature. A solid-solid phase transition is also observed ($T=48\text{K}$), but of a significantly different nature than in the previous studies of Vycor. Not only does the FCC structure fail to appear, we see the disappearance of structure altogether. At high Q , however, the background x-ray intensity is the same as in the high temperature solid phase (DHCP). This indicates, using the f sum rule, that the same amount of Ar is present in the probed region. However, the dramatically different scattering observed in this regime indicates that the Ar cannot be in a liquid or glass phase inside the pores, where the scattering would be similar to that observed at 85K . It is also important to note that the Ar cannot have formed a different crystalline solid phase, or the scattering would show diffraction peaks. The only remaining possibility is that a substantial amount of Ar migrates out of the pores and distributes itself on the surface of the sol-gel powder particle. The total amount of material in the scattering volume would remain fixed. However, the scattering would show little structure since it would be due only to

a layer of Ar distributed over the entire surface of the particle.

The difference in the behavior of the Vycor and sol-gel samples, given their structural similarities, is quite mysterious. The most significant difference between the physical samples, on which the measurements were carried out, was their size. The Vycor was a monolithic piece with a thickness of 1.2mm , while the sol-gel was a powder with a particle diameter of $11\mu\text{m}$. Conventional wisdom would indicate that this difference would be irrelevant. However, given the strange behavior observed, the original Vycor sample was crushed to a particle size similar to that of the sol-gel. Figure 3 shows the diffraction measurements performed on the powdered Vycor. These measurements are now nearly identical to those seen in the sol-gel glass, indicating that the transition is a result of the sample size.

Small angle x-ray scattering (SAXS) measurements were carried out to confirm that the Ar was leaving the pores. To perform these measurements, the incident and detector slits were closed to $1\times 2\text{mm}$ and $0.5\times 2\text{mm}$, respectively. This provides a minimum Q of 0.0088\AA^{-1} , which corresponds to a maximum length scale of $\sim 700\text{\AA}$. Above the transition, the SAXS measurements are temperature and time independent in the solid. However, below the transition, as shown in Figure 4, the SAXS studies show a time dependent behavior. This supports our view that Ar is leaving the pores and adsorbing onto the outer surface of the glass powder particles. This motion of the Ar, so far below the bulk freezing temperature, can only be explained if the mobility of the solid increases dramatically. The rapid onset of this increased mobility, which occurs over less than a degree, suggests that a transition, from a traditional low-mobility solid to a solid with an anomalously large mobility, has occurred. The time constant for this mobility is on the order of 5000 seconds, corresponding to a diffusion rate of $\sim 10^{-14}\text{ m}^2/\text{s}$, which is large compared to what would be expected in a solid at this temperature.

This transition, where the solid becomes mobile at low temperatures, has not heretofore been observed. However, it does provide an insight into the solid-solid transition reported by Brown, et. al.⁵. Their sample was simply too large for the Ar to leave the pores in a reasonable amount of time. In light of the diffusion rate reported here for our measurements, it would have taken ~ 2 years for Brown to have seen the same effect in his monolithic Vycor sample. However, the enhanced mobility in the monolithic piece did allow the material to rearrange and form FCC crystallites that spanned several pores.

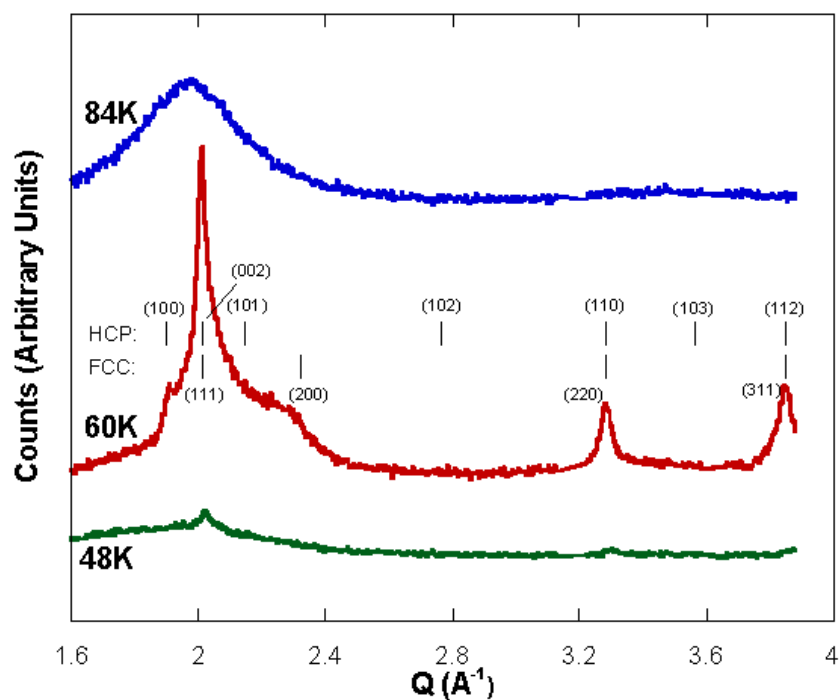


Figure 2: Diffraction measurements of Ar in sol-gel at 84K, 60K, and 48K with the background subtracted. Note the disappearance of structure in the low T solid.

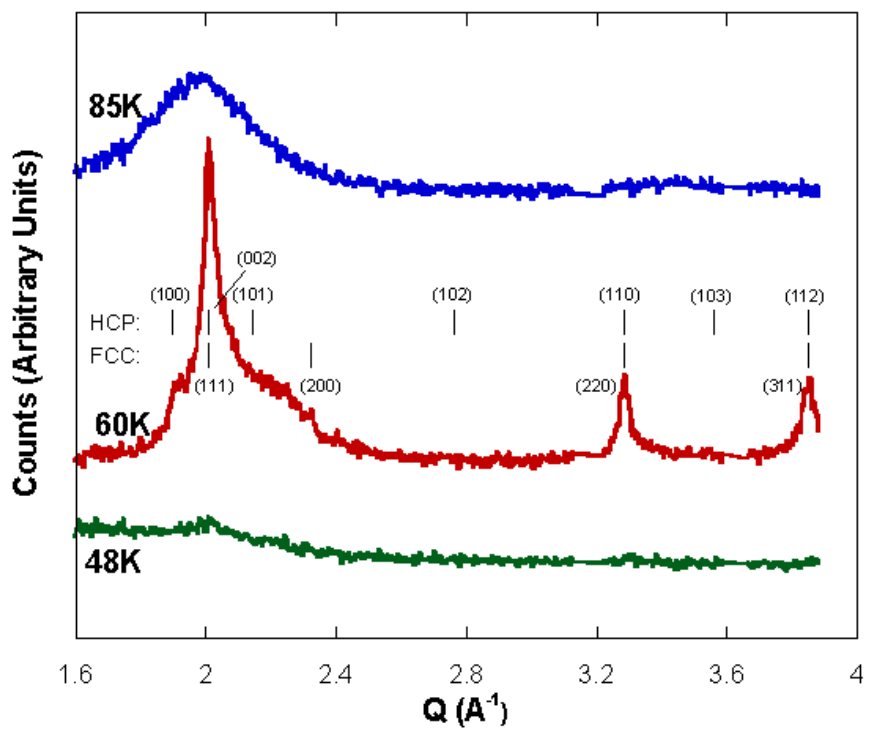


Figure 3: Diffraction measurements of Ar in powdered Vycor at 85K, 60K, and 48K with the background subtracted.

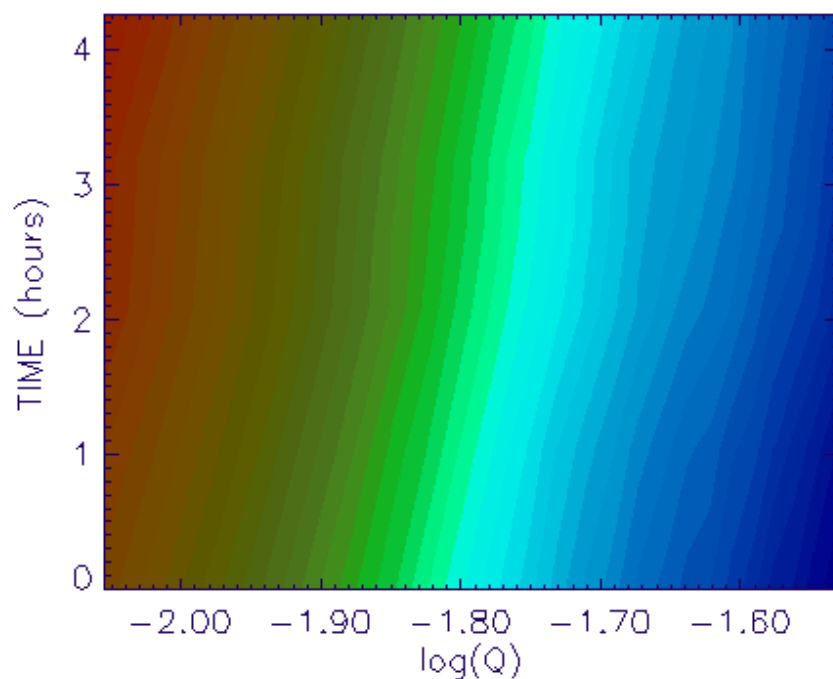


Figure 4: Small angle x-ray scattering measurements of Ar in sol-gel. This contour plot shows intensity as a function of both time and $\log Q$, where the red is at a greater intensity and the blue at a lesser. At a fixed Q , the intensity increases as a function of time.

Acknowledgements:

This work is supported by the NSF under Grant No. DMR 9970126.

References

1. Kumzerov, Yu. A., Nabereznov, A.A., Vakhrushev, S.B. & Savenko, B.N. Freezing and melting of mercury in porous glass. *Phys. Rev. B* **52**, 4772 (1995).
2. Bellissent-Funel, M.-C., Lal, J. & Bosio, L. Structural study of water confined in porous glass by neutron scattering. *J. Chem. Phys.* **98 No. 5**, 4246-4252 (1993).
3. Wang, Y., Snow, W.M. & Sokol, P.E. Structure and Phase Transitions of D₂ in Vycor. *J. Low Temp. Phys.* **101**, 929 (1995).
4. Schirato, B.S., Fang, M.P., Sokol, P.E. & Komarneni, S. The Structure of Confined Oxygen in Silica Xerogels. *Science* **267**, 369-371 (1995).
5. Brown, D.W., Sokol, P.E. & Ehrlich, S.N. New Disorder Induced Phase Transitions of Classical Rare Gases in Porous Vycor Glass. *Phys. Rev. Lett.* **81**, 1019-1022 (1998).
6. Awschalom, D.D. & Warnock, J. Supercooled liquids and solids in porous glass. *Phys. Rev. B* **35**, 6779-6770 (1987).
7. Berg, K.A., Witt, R.H. & Derolf, R. US Patent #5,149,553. PQ Corporation. 700,205(5,149,553). 1991. Pennsylvania, USA.